SARS-CoV-2 structure and replication characterized by *in situ* cryo-electron tomography

Steffen Klein[1,2,#], Mirko Cortese[3,#], Sophie L. Winter[1,2,#], Moritz Wachsmuth-Melm[1,2], Christopher J. Neufeldt[3], Berati Cerikan[3], Megan L. Stanifer[3], Steeve Boulant[4], Ralf Bartenschlager[3,5,6,*], Petr Chlanda[1,2,*]

[1] Schaller Research Groups, Department of Infectious Diseases, Virology, Heidelberg University, Heidelberg, Germany. [2] Research Group "Membrane Biology of Viral Infection", Department of Infectious Diseases, Virology, Heidelberg University, Heidelberg, Germany. [3] Department of Infectious Diseases, Molecular Virology, Heidelberg University, Heidelberg, Germany. [4] Research Group "Host/Pathogen Interactions at Intestinal Epithelial Surfaces", Department of Infectious Diseases, Virology, Heidelberg University, Heidelberg, Germany. [5] Division Virus-Associated Carcinogenesis, German Cancer Research Center, Heidelberg, Germany. [6] German Center for Infection Research (DZIF), (Heidelberg Partner Site), Heidelberg, Germany.

[#] equal contribution

[*] correspondence to: petr.chlanda@bioquant.uni-heidelberg.de, ralf.bartenschlager@med.uni-heidelberg.de

Severe acute respiratory syndrome coronavirus 2 (SARS-CoV-2), the causative agent of the COVID19 pandemic, is a highly pathogenic β-coronavirus. As other coronaviruses, SARS-CoV-2 is enveloped and remodels intracellular membranes for genome replication and assembly. Here, we report critical insights into the budding mechanism of the virus and provide structural details of virions and virus induced double-membrane vesicles by *in situ* cryo-electron tomography. We directly visualized double-stranded RNA within double-membrane vesicles, forming a loosely organized network with frequent RNA branching consistent with template-directed RNA synthesis intermediates. Our data indicate that membrane bending is orchestrated by the spike trimer and viral ribonucleoprotein complex recruitment into virion budding sites, suggesting the synergistic interplay of both viral components as a possible drug target for intervention.

Coronaviridae is a large family of positive-sense single-stranded RNA ((+)ssRNA) viruses that infect a broad range of vertebrate hosts. β-coronaviruses, including SARS-CoV-1 and Middle Eastern Respiratory Virus (MERS-CoV) are highly contagious pathogens that can cause severe lower respiratory infections. At the end of 2019, SARS-CoV-2 emerged in the city of Wuhan, China, likely through zoonotic transmission via a bat reservoir and a still unidentified intermediate host that subsequently led to a pandemic (*1*), accumulating to date to over 8 million cases and close to 500,000 deaths worldwide (*2*).

Cryo-electron microscopy studies of SARS-CoV-1 and the closely related murine hepatitis virus (MHV) show that the virions are predominantly spherical or ellipsoidal with an average envelope diameter between 80 and 90 nm (*3*). The main structural components of coronaviruses are the glycoprotein S, the transmembrane proteins M and E and the nucleoprotein N, which forms a viral ribonucleoprotein (vRNPs) complex with the viral RNA (vRNA). SARS-CoV-2 and SARS-CoV-1 S are structurally similar glycosylated homotrimers (*4*, *5*) that bind to the angiotensin-converting enzyme 2 (ACE2) receptor present on the cell surface of permissive cells (*6*). Similar to other (+)ssRNA viruses (*7*), coronaviruses modify cellular membranes to form double-membrane vesicles (DMVs), which are used as dedicated sites for vRNA replication (*8*). Several studies on β-coronaviruses SARS-CoV-1 and MERS-CoV that include electron tomography (ET) point towards DMVs being derived from ER cisternae in a process predominantly driven by the nonstructural protein 3 (nsp3) and nsp4 (*9*). In this model, the ER lumen constitutes the space between the DMV's inner and outer membrane, while the enclosed space is of cytoplasmic origin and enriched in double-stranded RNA (dsRNA) (*10*). Although the DMVs' outer membranes are interconnected through narrow pores, the inner membrane appears to be sealed, posing the important question of how RNA is transported through the two membranes into the cytoplasm. Virion assembly takes place on the cytoplasmic side of the ER-Golgi intermediate compartment (ERGIC) cisternae (*11*).

Here, we used cryo-ET on cryo-focused ion beam (cryo-FIB) milled lamellae or whole cell cryo-ET of various SARS-CoV-2 infected cell lines to structurally characterize DMV morphology, virus assembly, and extracellular virions close to their native state. In addition to commonly used monkey kidney derived VeroE6 cells, we included the human pulmonary cell lines Calu3 and an A549 derived cell line stably expressing the ACE2 receptor (A549-ACE2) that is

largely absent in naïve A549 cells (Fig S1A). Consistent with previous results on SARS-CoV-1 (*12*), we could show that exogenous expression of ACE2 renders A549 cells permissive for SARS-CoV-2 (Fig. S1B and C). Although ACE2 mRNA levels in A549-ACE2 cells were higher than in Calu3 and VeroE6 cells, VeroE6 and Calu3 cells showed a higher proportion of infected cells at 16 hours post infection (hpi) characterized by anti-dsRNA staining (Fig. S1D and E), indicating that ACE2 mRNA levels do not directly correlate with permissiveness of these cell lines to SARS-CoV2 infection.

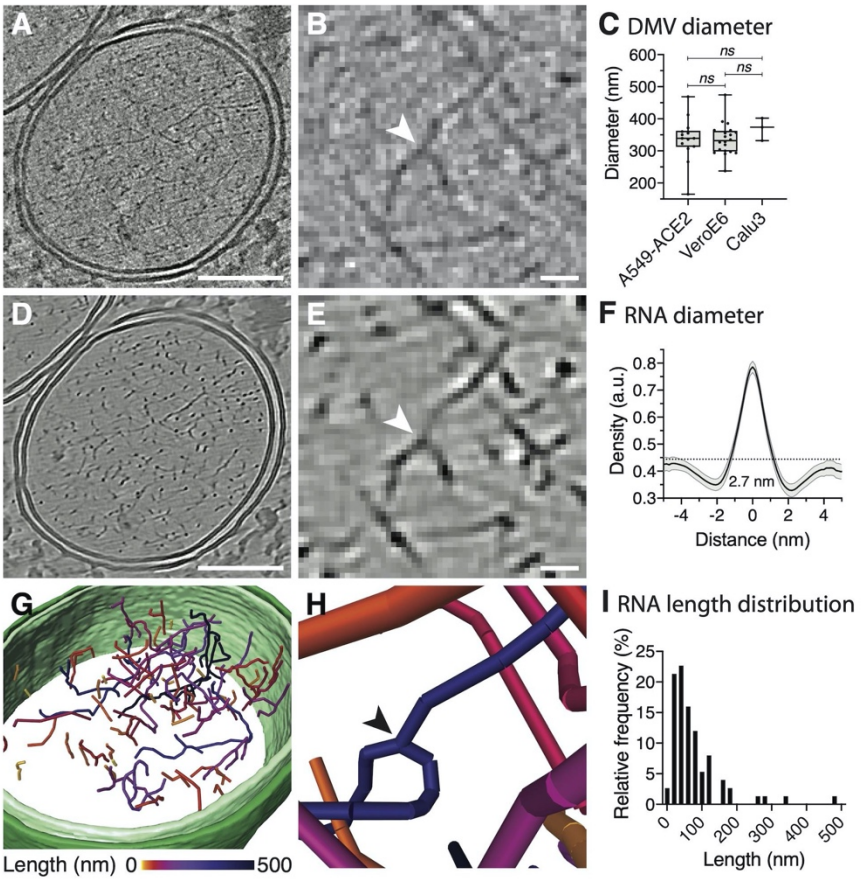

Fig. 1. Spatial distribution and length of RNA filaments. (**A**) Slice of a SIRT-like filtered tomogram of an A549-ACE2 cell infected with SARS-CoV2 showing a DMV. (**B**) Magnified slice showing filaments and a filament branching point (arrowhead) in detail. (**C**) Distribution of DMV inner membrane diameter in three different cell lines (A549-ACE2: n = 14; VeroE6: n = 20; Calu3: n = 3). Data is shown as Box and Whiskers plots indicating the median, 25% and 75% quantiles, minimum and maximum values and all data points. (**D** and **E**) Tomogram slices shown in (A and D) after content-aware denoising using cryo-CARE (*16*). (**F**) Average normalized density line profile of filament cross-sections with indicated standard deviation (n = 80 from two tomograms) and average grey value of the DMV interior (0.44 a.u., dotted line). (**G** and **H**) Manual segmentation of the denoised DMV (Movie S1), inner and outer membrane are represented in light and dark green, respectively. Individual segmented filaments are colored according to their length and a branching point is indicated by an arrowhead in the magnified segmentation image (H). (**I**) Histogram of RNA length (n = 75) with a bin size of 20 nm. Length of branched filament was calculated as a sum of all connected filaments. Scale bars: (A and D) 100 nm, (B and E) 10 nm.

DMVs and the RNA network

We first focused on the characterization of DMVs, which were found in all analyzed cell lines (Fig. S2), and on the visualization of RNA confined in the DMV interior. Cryo-ET revealed that both inner and outer DMV membranes appeared smooth and were separated by a variable luminal spacing of 18 nm (SD = 9 nm, n = 32) (Fig 1). DMV appearance and size distributions were similar in all infected cell lines with an inner average diameter of 336 nm (SD = 50 nm, n = 20) (Fig. 1C). This is in agreement with the diameter of the DMVs in SARS-CoV-1 infected VeroE6 cells, which was 300 ± 50 nm using the outer membranes (*10*). A network of thin and electron-dense filaments, presumably representing vRNA, was clearly observed in all DMVs (Fig. 1, S2). Individual vRNA filaments appeared smooth and did not organize into bundles or concentric layers (Fig. 1D and E, Movie S1) that were observed for the dsRNA of the Flock House Virus (*13*). The filaments had a uniform average diameter of 2.68 nm (SD = 0.23 nm, n = 80 from two tomograms) (Fig. 1F) and no electron-densities attributable to proteins attached to the fibers or to the inner DMV membrane were observed. The measured filament diameter corresponds well to the diameter of the A-form RNA double-stranded helix (*14*). Strikingly, we observed filament branching points reminiscent of transcription intermediates representing a template that is copied with newly synthesized RNA being displaced from the template (Fig. 1G and H). Individual filaments featured a highly variable length ranging from 8 – 487 nm with an average length of 76 nm (SD = 79 nm, n = 75) (Fig. 1I). The length distribution corresponds to 29 – 1739 base pairs taking into account the 0.28 nm rise per residue in the dsRNA A-helix (*14*). Considering that E and S, based on their gene length, would form 64 nm and 1070 nm long A-form helices, the observed filaments might represent dsRNA intermediates of subgenomic transcripts. In line with other reports, we were unable to localize an opening in the DMV

membranes such as a pore that would allow RNA trafficking between the DMV interior and the cytoplasm. Together, our observations show a DMV interior rich in dsRNA. Although DMVs might be a site of replication, it is as well possible that DMVs' purpose is to conceal dsRNA transcription and replication byproducts that would otherwise be recognized by pattern recognition receptors of the innate immune system. Interestingly, the vault complexes, that among other functions have a role in dsRNA or virus-induced proinflammatory response (*15*), were observed in the proximity of DMV membranes (Fig. S3A – F).

It has previously been shown that DMVs are part of a network and can fuse into multivesicular compartments (*10*). To provide further structural information on how DMV fusion is mechanistically governed, DMVs within close proximity to each other were analyzed (Fig. 2). Besides funnel-like connections (Fig. 2A), we observed tightly apposed DMVs where all four membranes were stacked forming a curved junction budding into juxtaposed DMVs (Fig. 2B and C). The junction appeared to be electron-dense, yet no particular features were found between the individual membranes. The membrane stack at the center of the junction had an average thickness of 19.4 nm (SD = 2.7 nm, n = 4), approximately conforming to four lipid bilayers, and an average diameter of 120 nm. Consistent with a recent study, we also found vesicle packets (VPs) containing two or more vesicles surrounded by one outer membrane, presumably a product of DMV-DMV fusion (Fig. 2D – F) (*17*). In one case, we observed that the inner membranes of the DMVs formed a junction that resulted in an opening between two fusing inner vesicles (Fig. 2F). Based on these observations, we propose that DMV homotypic fusion occurs through membrane stacking engaging both inner and outer membranes. Tight membrane apposition together with high curvature might energetically contribute to membrane fusion or to a membrane rupture followed by membrane resealing. Since DMV fusion leads to a minimization of membrane surface to volume ratio and the number of VPs increases during the infection (*17*), we speculate that DMV fusion is required for repurposing membranes for virion budding at advanced stages of the replication cycle, which is supported by

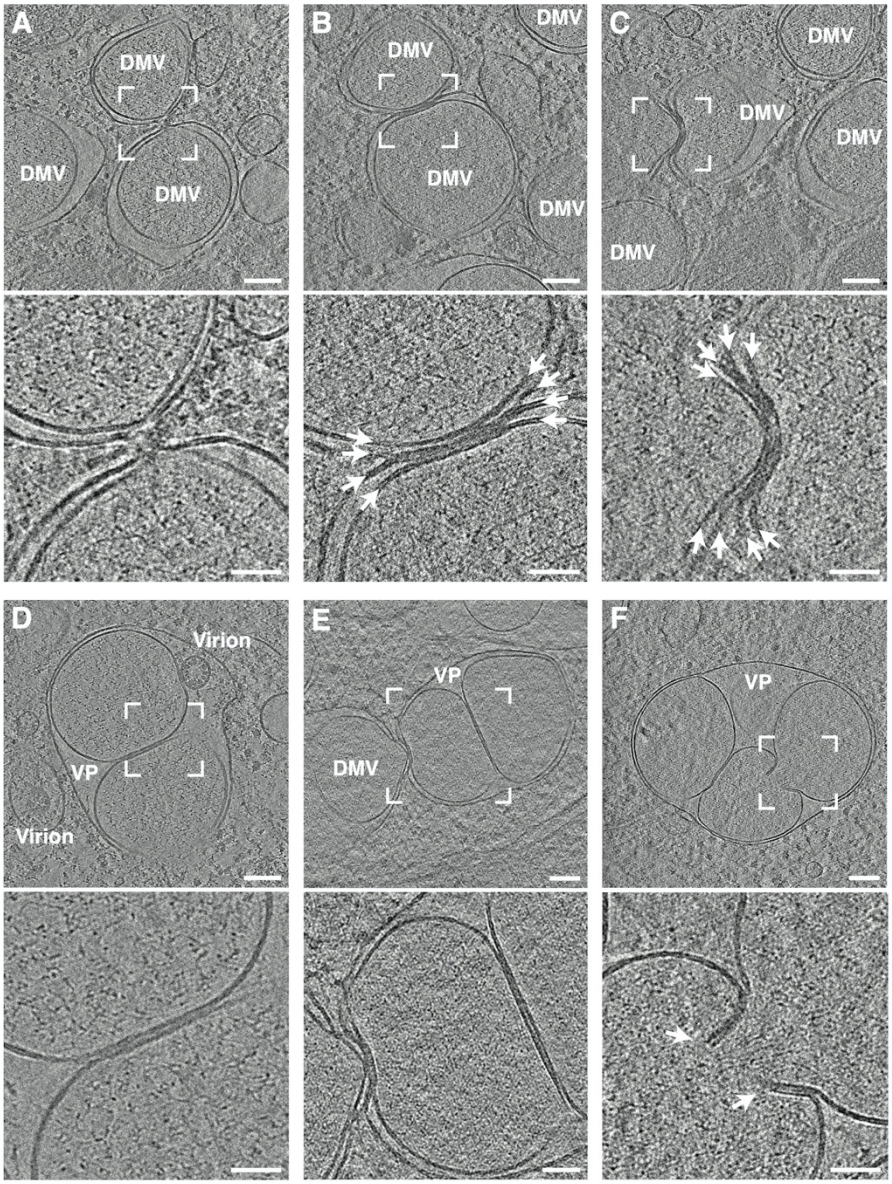

Fig. 2. Juxtaposed DMVs form membrane junctions that lead to homotypic fusion. Tomograms showing DMVs in VeroE6 (A – C) and Calu3 (D – F) cells at 16 hpi. For each tomogram, a magnified area is shown below and indicated as a white square. 10 slices of the tomogram were averaged. (**A**) DMV-DMV interaction via a constricted outer membrane connection. (**B** and **C**) Tightly apposed membrane stack composed of four membranes (arrows) of varying curvature between two juxtaposed DMVs. (**D**) VP containing two inner vesicles with a tight membrane-membrane contact. (**E**) DMV interaction with a VP containing two inner vesicles. (**F**) VPs containing four inner vesicles with tight contact and an opening aperture formed by two stacked membranes indicated by white arrows. Scale bars: (A – F) 100 nm, (magnified areas) 50 nm.

the observation of a fully assemble virion inside the VP lumen (Fig. 2D).

Virion assembly and structure of intracellular virions

The ERGIC constitutes the main assembly site of coronaviruses (*11*) and budding events have been described by EM studies (*10*, *18*, *19*). *In situ* cryo-ET allowed us here for the first time to study SARS-CoV-2 virion assembly in close to native conditions and enabled us to localize individual S trimers and vRNPs with high precision. Virus-budding was mainly clustered in regions with a high vesicle density and close to ER- and Golgi-like membrane arrangements (Fig. 3A and S4, Movies S2 and S3). S trimers were regularly found in low quantities with the ectodomain facing the ERGIC lumen. Even at high densities, in the absence of vRNPs, S trimer accumulation did not coincide with positive membrane curvature (Fig. 3B and C), indicating that S alone is unable to initiate virus budding. Early budding events with a positively curved membrane were decorated on the lumenal side with S and on the cytosolic side with vRNPs (Fig. 3D and E) in all observed events (n = 19), supporting the model where the viral transmembrane M protein acts as an organization assembly hub, interacting with both the S and the N protein (*20*, *21*). Budded virions that were located directly adjacent to the ERGIC membrane showed a polarized distribution of S trimers facing towards the ERGIC lumen (Fig. 3F). In contrast, virions that were more distant from the membrane showed a dispersed distribution of S (Fig. 3G) around the entire virion, indicating that S trimers are mobile on the virion envelope and redistribute during the budding process. Thus, the lattice between S – M – N may not be as well-defined as previously proposed (*22*).

We further analyzed the structure of intracellular virions. Notably, S trimers were not always oriented orthogonally to the membrane of the mostly spherical or ellipsoidal virions (Fig. 4A and B). Previous ultrastructural studies of other coronaviruses reported average virion diameters of 85 ± 5 nm for MHV (*3*) and 88 ± 6 nm for SARS-CoV-1 (*22*). We did not observe

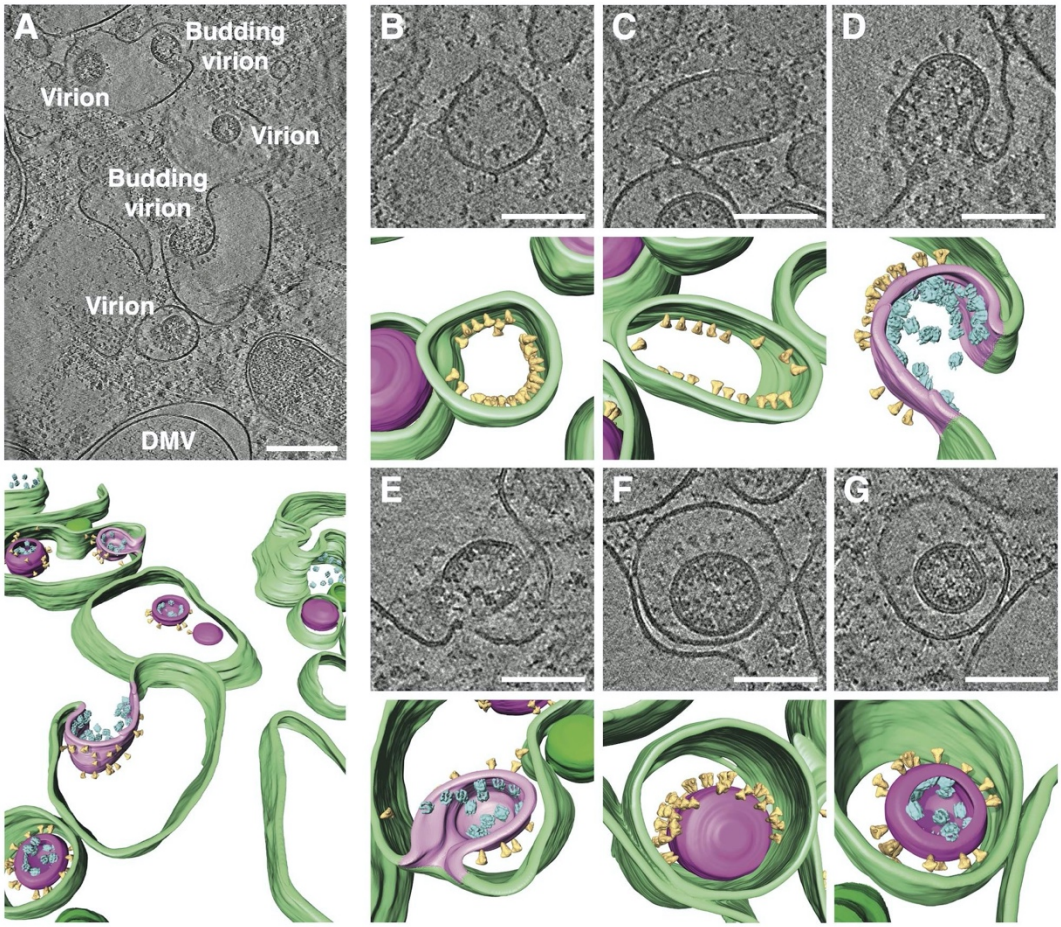

Fig. 3. SARS-CoV-2 virion budding and assembly at the ERGIC membrane. Different budding events captured in two tomograms (Fig. S4, Movies S2 and S3) of VeroE6 cells infected with SARS-CoV-2 at 16 hpi. A 3D volume rendering is shown for each area with cellular and viral membranes in green and magenta, respectively. S (yellow) and vRNPs (cyan) are represented as subtomogram averages. The S and vRNP locations correspond to the location in the tomogram, vRNP orientations were randomized. A non-local means filter was applied, and 20 slices were averaged. (**A**) Overview of budding events at the ERGIC membrane and intracellular released virions inside the ERGIC lumen are indicated. (**B** and **C**) Accumulated S at the lumenal side of the ERGIC membrane. (**D** and **E**) Early virion budding stage with S and vRNPs accumulated at the lumenal and cytosolic ERGIC membrane, respectively. (**F**) Assembled virion in the ERGIC lumen in close proximity to the membrane, showing a polarized distribution of S. (**G**) Assembled virion further away from the membrane with redistributed S. Scale bars (A) 200 nm, (B – G) 100 nm.

significant differences in the average diameters of virions derived from the three cell lines (Fig. 4C) and calculated an average diameter of 89.8 nm (SD = 13.7 nm, n = 74). Subtomogram averaging (STA) of 219 individual S trimers yielded a low resolution structure with a total height of approximately 25 nm measured from the virion envelope and a total width of 13 nm (Fig. 4D – F, S5). The density map featured a well-defined trimeric structure with a height of 16 nm which is in agreement with the published structure solved by single particle analysis of the purified S ectodomain in pre-fusion conformation truncated at serine residue 1147 (PDB:6VXX) (*4*), indicating that the S trimer is fully formed during virion budding. The approximately 9 nm long gap between the trimeric density and the virion envelope that can be attributed to the triple-stranded coiled-coil heptad repeat 2 (HR2) was not resolved, most likely because of the high flexibility of S. To estimate the number of S trimers per virion, we extracted the 3D coordinates of all identifiable S trimers on nine intracellular virions and determined the average nearest-neighbor distance to be 23.6 nm (SD = 8.1 nm, n = 100) (Fig. 4G). Based on the mathematical problem of arranging any number of points on a sphere to maximize their minimum distance, known also as the 'Tammes Problem' (*23*, *24*), we estimated the average number of S trimers per virion to be 48 with a range of 25 – 127 (Fig. S6). This is in line with our observation of heterogeneous S trimer densities on the surface of virions and concurs with previously reported estimates of 50 – 100 S trimers per virion (*22*, *25*).

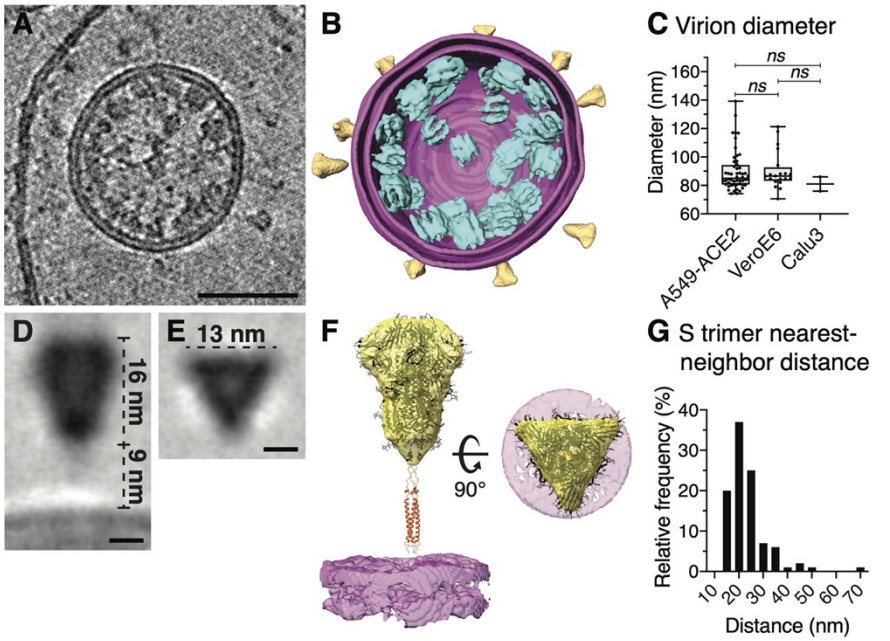

Fig. 4. Structural analysis of intracellular virions. (**A**) Tomogram showing an intracellular virion of VeroE6 cells infected with SARS-CoV-2 at 16 hpi. 20 slices of the tomogram were averaged and a median filter (radius = 1 pixel) was applied. (**B**) 3D volume rendering of (A) with the viral envelope shown in magenta, with both leaflets of the membrane resolved. S (yellow) and vRNPs (cyan) are represented as subtomogram averages. The S and vRNP locations correspond to the location in the tomogram, vRNP orientations were randomized. (**C**) Distributions of intracellular virion diameters measured in A549-ACE2 (n = 52), VeroE6 (n = 20) and Calu3 cells (n = 3). Box and Whiskers plots indicate the median, 25% and 75% quantiles and minimum and maximum values as well as all data points. Unpaired t-test showed no significant differences between the diameter of intracellular virions found in the three different cell lines. (**D** and **E**) Central longitudinal (D) and cross-sectional slice (E) showing the subtomogram average of the S trimer. (**F**) Orthogonal views of the S trimer subtomogram average (yellow) and the virion envelope (magenta). Fitted structure of the S trimer ectodomain (PDB:6VXX) (*4*) and the HR2 domain of SARS-CoV-1 (PDB:2FXP) (*26*) are shown in black and orange, respectively (Movie S4). (**G**) Plot showing the distribution of S nearest-neighbor distances (n = 100) on the surface of virions with an average of 23.6 nm (SD = 8.1 nm, n = 100). Scale bars: (A) 50 nm (D and E) 5 nm.

Structure of extracellular virions

We next analyzed extracellular virions in the vicinity of infected cells to provide insights into conformational changes of the S trimers and vRNP structure. Virions were found close to the plasma membranes of all host cells, albeit with notable differences in the number of virions directly attached. We found few virions around A549-ACE2 cells, all of which appeared to directly interact with the cell surface (Fig. 5A). In contrast, a high density of virions from VeroE6 cells were covering the surface of filopodia and protrusions that interconnected neighboring cells (Fig. 5B, S7). These observations are reminiscent of the cell-to-cell transmission via viral surfing as reported for HIV (*27*) and could suggest a yet undescribed mode of transmission for SARS-CoV-2. In contrast, no virions were found attached to Calu3 cells (Fig. 5C). Differences in the number of virions attached to the analyzed cell lines might be explained by different levels of ACE2 receptors controlled by surface proteases such as TMPRSS2 or ADAM17 (*28*). It is plausible that ACE2 levels on the cell surface does not only influence virion entry but also virion release.

In agreement with our observations in intracellular virions, extracellular virions released from VeroE6 cells

were studded with S trimers in pre-fusion conformation that were often tilted and had an average length of 23.4 nm (SD = 2.3 nm, n = 48) (Fig. 5E). Noticeably, extracellular virions from A549-ACE2 cells exhibited almost exclusively thin, rod-shaped S trimers resembling the post-fusion conformation (*29*, *30*) with an overall length of 23.2 nm (SD = 2.3 nm, n = 8) and thickness of 3.8 nm (SD = 0.7 nm, n = 9) (Fig. 5D). Virions from Calu3 cells displayed a mixture of both spike conformations (Fig. 5F). The host cell-type dependent difference in the number of pre-fusion and post-fusion conformations may be explained by different levels of TMPRSS2 proteases (*31*) and ACE2 receptors that trigger S conformational changes. Consistently, S trimers in post-fusion conformation were primarily detected on virions directly interacting with A549-ACE2 cells expressing high levels of ACE2 (Fig. 5D, S1). In contrast, S present on virions in ACE2 low-expressing VeroE6 cells (Fig. S1) were almost exclusively in pre-fusion conformation.

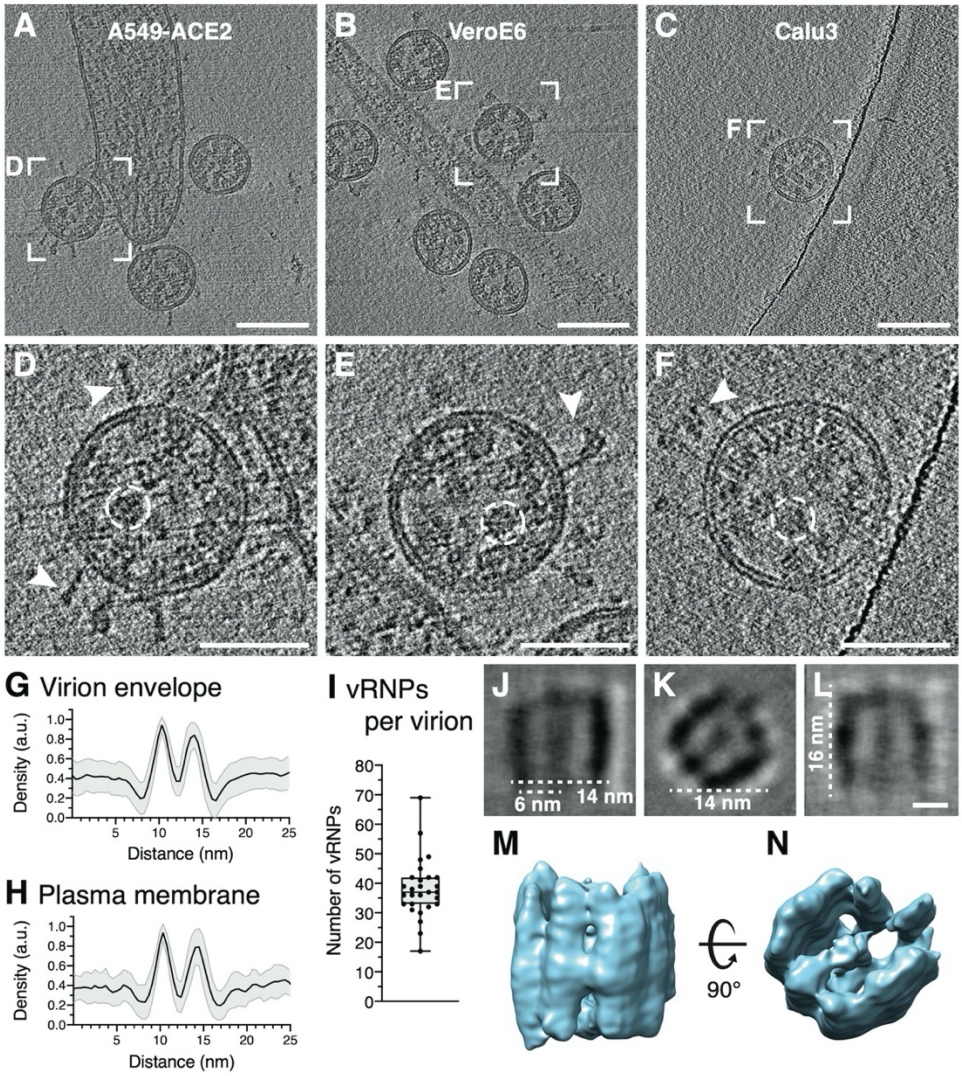

Fig. 5. Structural analysis of extracellular virions. (**A** – **C**) Slices of tomograms showing extracellular virions released from A549-ACE2, VeroE6 and Calu3 cells, respectively, with indicated virions magnified in (**D** – **F**). For better visualization, 10 slices were averaged. Exemplarily, S glycoproteins are marked with white arrowheads, vRNP complexes are encircled with dashed lines. (**G** and **H**) Plot profile through the membrane envelope of virions from VeroE6 cells (G) and adjacent plasma membrane (H) to determine monolayer separation (n = 129 and 49, respectively, SD indicated). (**I**) Number of vRNP complexes per virion (n = 28) released from VeroE6 cells. Data is represented as a Box and Whiskers plot indicating the median, 25% and 75% quantiles and minimum and maximum values as well as all data points. (**J** – **L**) Slices through the STA of vRNP complexes found in 15 tomograms from VeroE6 cells with (J) representing the XZ-slice through the center of the vRNP, (K) showing the XY-slice along the long axis of the vRNP and (L) displaying the YZ-view. (**M** and **N**) Isosurface representation of the subtomogram average (Movie S5) shown from the side (M) and top view (N). Scale bars (A – C) 100 nm, (D – F) 50 nm, (L) 5 nm.

Based on a previous cryo-ET study revealing an unusual membrane thickness of MHV virions of 7 – 8 nm (*3*), we measured the lipid bilayer separation of SARS-CoV-2 virions. Density line profiles across the membranes showed a phospholipid monolayer separation of 3.6 nm (SD = 0.5 nm, n = 129) (Fig. 5G) whereas the plasma membrane was slightly but significantly thicker (3.9 nm, SD = 0.5 nm, n = 49) as evaluated by a two-sided t-test (p = 0.003) (Fig. 5H). This indicates that membrane thickness is not increased by the viral transmembrane proteins M and E in SARS-CoV-2. Extracellular virions displayed on average 38 vRNPs per virion (SD = 10, n = 28) (Fig. 5I), suggesting that each vRNP contains approximately 800 bases of the SARS-CoV-2 ~30kb genome. vRNPs associated with viral envelopes were often aligned in stacks, forming filaments with a width of approximately 14 nm (Fig. 5F, S8), indicating a preferred stacking orientation of vRNPs. STA of 1570 vRNPs yielded a compact, cylindrical assembly of 16 nm in length and a quasi-circular base with an approximate diameter of 14 nm (Fig. 5J and K, S9, Movie S5). The assembly is composed of parallel-stacked, pillar-shaped densities, presumably formed

by multiple linearly aligned N proteins. Pillar-shaped densities form two densely packed curved walls opposing each other and surrounding a central density, separated from the walls by 6 nm (Fig. 5J and L). While the walls are connected by an additional pillar on one side, the other side appears more flexible with two pillar-like densities creating an opening. Previous EM studies of vRNPs isolated from MHV and SARS-CoV-1 virions described a helical nucleocapsid (*3*, *32*) or a coiled vRNP that forms a membrane-proximal lattice (*22*). MHV virions analyzed by cryo-ET have been described to contain granular densities and quasi-circular density profiles of 11 nm in diameter, which appear similar to the densities found in our study (*3*). We propose that vRNPs are separate complexes organized like 'beads on a string' that allows for efficient packing of the unusually large vRNA genome into the virus particles while maintaining high sterical flexibility between the individual vRNPs required during their incorporation into budding virions.

Concluding remarks

Our report provides the first *in situ* cryo-ET analysis of coronaviruses at high preservation levels. Direct visualization of RNA filaments inside the replication-associated DMVs unveils dsRNA as the major constituents of the DMV interior and filament branching points suggestive of RNA *in statu nascendi.* Given the absence of a pore on the DMV membrane and the lack of protein densities in the DMV interior, it is also cogitable that the DMV interior rather serves to selectively accumulate dsRNA intermediates to evade the antiviral innate immune response, whereas vRNA replication might be associated with the cytosolic side of the DMV proximal membrane. Our data indicate that S trimers alone do not induce membrane curvature during budding but are remarkably motile and flexible and the increased exposure of the conserved stem region renders it a promising candidate for development of coronavirus pan-neutralizing antibodies. We propose that the interplay between S trimers and vRNPs is inducing membrane curvature during virion budding, emphasizing that the vRNP membrane association might be a promising target to inhibit virus assembly.

Acknowledgments

We thank Dr. Manfred Frey, Mannheim for kindly providing Calu3 cell line, Dr. Christian Drosten and European Virus Archive-Global for providing SARS-CoV2 virus, and Christian Willig for the help with the error propagation calculation. We thank Dr. Ivonne Morales and Dimitris Papagiannidis for critical reading of the manuscript. We would like to acknowledge microscopy support from the Infectious Diseases Imaging Platform (IDIP) at the Center for Integrative Infectious Disease Research Heidelberg. We would like to acknowledge access to the infrastructure and support provided by the Cryo-EM Network at the Heidelberg University (HD-cryoNet). **Funding:** This work was supported by a research grant from the Chica and Heinz Schaller Foundation (Schaller Research Group Leader Programme) to P.C., S.L.W. and M.W-M. and by the Deutsche Forschungsgemeinschaft (DFG, German Research Foundation), project number 240245660 – SFB 1129 to P.C., S.K., S.B. and R.B. Work of R.B. was additionally funded by the DFG, project number 112927078 – TRR 83. S.B. is supported by the Heisenberg program, project number 415089553 and M.L.S. is supported by the DFG, project number 41607209. **Authors contributions:** Sample preparation: S.K., M.C., S.L.W., M.W-M., C.N., B.C., M.L.S., S.B., P.C; study conceptualization and design: S.K., M.C., S.L.W., P.C., R.B.; data collection: S.K., M.C., S.L.W., M.W-M., P.C.; analysis: S.K., M.C., S.L.W., M.W-M., P.C., preparation of the manuscript: S.K., M.C., S.L.W, M.W-M, P.C., R.B. **Competing interests:** The authors declare that there are no competing interests regarding the publication of this article.

References

1. P. Zhou, X.-L. Yang, X.-G. Wang, B. Hu, L. Zhang, W. Zhang, H.-R. Si, Y. Zhu, B. Li, C.-L. Huang, H.-D. Chen, J. Chen, Y. Luo, H. Guo, R.-D. Jiang, M.-Q. Liu, Y. Chen, X.-R. Shen, X. Wang, X.-S. Zheng, K. Zhao, Q.-J. Chen, F. Deng, L.-L. Liu, B. Yan, F.-X. Zhan, Y.-Y. Wang, G.-F. Xiao, Z.-L. Shi, A pneumonia outbreak associated with a new coronavirus of probable bat origin. *Nature*. **579**, 270–273 (2020).
2. E. Dong, H. Du, L. Gardner, An interactive web-based dashboard to track COVID-19 in real time. *Lancet Infect. Dis.* **20**, 533–534 (2020).
3. M. Bárcena, G. T. Oostergetel, W. Bartelink, F. G. A. Faas, A. Verkleij, P. J. M. Rottier, A. J. Koster, B. J. Bosch, Cryo-electron tomography of mouse hepatitis virus: Insights into the structure of the coronavirion. *Proc. Natl. Acad. Sci. U. S. A.* **106**, 582–587 (2009).
4. A. C. Walls, Y.-J. Park, M. A. Tortorici, A. Wall, A. T. McGuire, D. Veesler, Structure, Function, and Antigenicity of the SARS-CoV-2 Spike Glycoprotein. *Cell*. **181**, 281–292.e6 (2020).
5. F. Li, Structure, Function, and Evolution of Coronavirus Spike Proteins. *Annu Rev Virol*. **3**, 237–261 (2016).
6. M. Hoffmann, H. Kleine-Weber, S. Schroeder, N. Krüger, T. Herrler, S. Erichsen, T. S. Schiergens, G. Herrler, N.-H. Wu, A. Nitsche, M. A. Müller, C. Drosten, S. Pöhlmann, SARS-CoV-2 Cell Entry Depends on ACE2 and TMPRSS2 and Is Blocked by a Clinically Proven Protease Inhibitor. *Cell*. **181**, 271–280.e8 (2020).
7. I. Romero-Brey, R. Bartenschlager, Membranous replication factories induced by plus-strand RNA viruses. *Viruses*. **6**, 2826–2857 (2014).
8. E. J. Snijder, R. W. A. L. Limpens, A. H. de Wilde, A. W. M.

de Jong, J. C. Zevenhoven-Dobbe, H. J. Maier, F. F. G. A. Faas, A. J. Koster, M. Bárcena, A unifying structural and functional model of the coronavirus replication organelle: tracking down RNA synthesis. *Microbiology* (2020).
9. D. Oudshoorn, K. Rijs, R. W. A. L. Limpens, K. Groen, A. J. Koster, E. J. Snijder, M. Kikkert, M. Bárcena, Expression and Cleavage of Middle East Respiratory Syndrome Coronavirus nsp3-4 Polyprotein Induce the Formation of Double-Membrane Vesicles That Mimic Those Associated with Coronaviral RNA Replication. *MBio*. **8** (2017).
10. K. Knoops, M. Kikkert, S. H. E. van den Worm, J. C. Zevenhoven-Dobbe, Y. van der Meer, A. J. Koster, A. M. Mommaas, E. J. Snijder, SARS-coronavirus replication is supported by a reticulovesicular network of modified endoplasmic reticulum. *PLoS Biol.* **6**, e226 (2008).
11. C. A. M. de Haan, P. J. M. Rottier, in *Virus Structure and Assembly* (Elsevier, 2005), vol. 64 of *Advances in Virus Research*, pp. 165–230.
12. E. C. Mossel, C. Huang, K. Narayanan, S. Makino, R. B. Tesh, C. J. Peters, Exogenous ACE2 expression allows refractory cell lines to support severe acute respiratory syndrome coronavirus replication. *J. Virol.* **79**, 3846–3850 (2005).
13. K. J. Ertel, D. Benefield, D. Castaño-Diez, J. G. Pennington, M. Horswill, J. A. den Boon, M. S. Otegui, P. Ahlquist, Cryo-electron tomography reveals novel features of a viral RNA replication compartment. *Elife*. **6** (2017).
14. J. R. Arias-Gonzalez, Single-molecule portrait of DNA and RNA double helices. *Integr. Biol.* . **6**, 904–925 (2014).
15. N. Peng, S. Liu, Z. Xia, S. Ren, J. Feng, M. Jing, X. Gao, E. A. C. Wiemer, Y. Zhu, Inducible Major Vault Protein Plays a Pivotal Role in Double-Stranded RNA- or Virus-Induced Proinflammatory Response. *J. Immunol.* **196**, 2753–2766 (2016).
16. T.-O. Buchholz, A. Krull, R. Shahidi, G. Pigino, G. Jékely, F. Jug, Content-aware image restoration for electron microscopy. *Methods Cell Biol.* **152**, 277–289 (2019).
17. N. S. Ogando, T. J. Dalebout, J. C. Zevenhoven-Dobbe, R. W. Limpens, Y. van der Meer, L. Caly, J. Druce, J. J. C. de Vries, M. Kikkert, M. Bárcena, I. Sidorov, E. J. Snijder, SARS-coronavirus-2 replication in Vero E6 cells: replication kinetics, rapid adaptation and cytopathology. *Microbiology* (2020).
18. K. McIntosh, S. Perlman, Coronaviruses, including severe acute respiratory syndrome (SARS) and Middle East respiratory syndrome (MERS). *Mandell, Douglas, and Bennett's Principles and Practice of Infectious Diseases, Updated Edition. 8th ed. Philadelphia, PA: Elsevier Saunders* (2015).
19. S. Stertz, M. Reichelt, M. Spiegel, T. Kuri, L. Martínez-Sobrido, A. García-Sastre, F. Weber, G. Kochs, The intracellular sites of early replication and budding of SARS-coronavirus. *Virology*. **361**, 304–315 (2007).
20. G. J. Godeke, C. A. de Haan, J. W. Rossen, H. Vennema, P. J. Rottier, Assembly of spikes into coronavirus particles is mediated by the carboxy-terminal domain of the spike protein. *J. Virol.* **74**, 1566–1571 (2000).
21. D. Escors, J. Ortego, H. Laude, L. Enjuanes, The membrane M protein carboxy terminus binds to transmissible gastroenteritis coronavirus core and contributes to core stability. *J. Virol.* **75**, 1312–1324 (2001).
22. B. W. Neuman, B. D. Adair, C. Yoshioka, J. D. Quispe, G. Orca, P. Kuhn, R. A. Milligan, M. Yeager, M. J. Buchmeier, Supramolecular architecture of severe acute respiratory syndrome coronavirus revealed by electron cryomicroscopy. *J. Virol.* **80**, 7918–7928 (2006).
23. P. M. L. Tammes, On the origin of number and arrangement of the places of exit on the surface of pollen-grains. *Recueil des travaux botaniques néerlandais*. **27**, 1–84 (1930).
24. E. B. Saff, A. B. J. Kuijlaars, Distributing many points on a sphere. *Math. Intelligencer*. **19**, 5–11 (1997).
25. B. W. Neuman, G. Kiss, A. H. Kunding, D. Bhella, M. F. Baksh, S. Connelly, B. Droese, J. P. Klaus, S. Makino, S. G. Sawicki, S. G. Siddell, D. G. Stamou, I. A. Wilson, P. Kuhn, M. J. Buchmeier, A structural analysis of M protein in coronavirus assembly and morphology. *J. Struct. Biol.* **174**, 11–22 (2011).
26. S. Hakansson-McReynolds, S. Jiang, L. Rong, M. Caffrey, Solution structure of the severe acute respiratory syndrome-coronavirus heptad repeat 2 domain in the prefusion state. *J. Biol. Chem.* **281**, 11965–11971 (2006).
27. W. Mothes, N. M. Sherer, J. Jin, P. Zhong, Virus cell-to-cell transmission. *J. Virol.* **84**, 8360–8368 (2010).
28. A. Heurich, H. Hofmann-Winkler, S. Gierer, T. Liepold, O. Jahn, S. Pöhlmann, TMPRSS2 and ADAM17 cleave ACE2 differentially and only proteolysis by TMPRSS2 augments entry driven by the severe acute respiratory syndrome coronavirus spike protein. *J. Virol.* **88**, 1293–1307 (2014).
29. A. C. Walls, M. A. Tortorici, J. Snijder, X. Xiong, B.-J. Bosch, F. A. Rey, D. Veesler, Tectonic conformational changes of a coronavirus spike glycoprotein promote membrane fusion. *Proc. Natl. Acad. Sci. U. S. A.* **114**, 11157–11162 (2017).
30. W. Song, M. Gui, X. Wang, Y. Xiang, Cryo-EM structure of the SARS coronavirus spike glycoprotein in complex with its host cell receptor ACE2. *PLoS Pathog.* **14**, e1007236 (2018).
31. S. Matsuyama, N. Nao, K. Shirato, M. Kawase, S. Saito, I. Takayama, N. Nagata, T. Sekizuka, H. Katoh, F. Kato, M. Sakata, M. Tahara, S. Kutsuna, N. Ohmagari, M. Kuroda, T. Suzuki, T. Kageyama, M. Takeda, Enhanced isolation of SARS-CoV-2 by TMPRSS2-expressing cells. *Proc. Natl. Acad. Sci. U. S. A.* **117**, 7001–7003 (2020).
32. M. Gui, X. Liu, D. Guo, Z. Zhang, C.-C. Yin, Y. Chen, Y. Xiang, Electron microscopy studies of the coronavirus ribonucleoprotein complex. *Protein Cell*. **8**, 219–224 (2017).